Supporting Information

An Integrated Framework for Assessing Impacts of CO_2 Leakage on Groundwater Quality and Monitoring-Network Efficiency: Case Study at a CO_2-EOR site

Changbing Yang[†]*, Susan D. Hovorka[†], Ramón H. Treviño[†], and Jesus Delgado-Alonso[‡]

*Corresponding author: Changbing.yang@beg.utexas.edu; Phone: (512) 471-4364, Fax: (512) 471-0140

AUTHOR ADDRESS

[†]Bureau of Economic Geology, The University of Texas at Austin, Austin, Texas, 78759, United States

[‡]Intelligent Optical Systems Inc., Torrance, California, 90505, United States

Environmental Science & Technology, document prepared 06/03/2015

Summary, 27 pages

The supporting information includes three sections: S1 includes 12 supplementary figures, S2 lists 5 supplementary tables and S3 presents impacts of dispersion coefficient, groundwater flow direction and aquifer heterogeneity on monitoring efficiency of a groundwater monitoring network at the CO_2-EOR site.

S1: Supplementary figures.

Figure S1. Plot of the CO_2–EOR site, the Cranfield oil and gas field, located at about 25 km east of the city of Natchez, Adams County, Mississippi. In the plot, circles are plugged and abandoned (P&A) wells and triangles represent existing groundwater wells in the shallow aquifer. The rectangle with dash lines represents the approximate location of the CO_2-EOR site and the solid triangle represents the monitoring well (UM-1) drilled into the sand unit of the Catahoula Formation and cored for aquifer sediments, as well as for the push-pull test.

Figure S2. Model domain for reactive transport modeling (RTM) of (a) the single-well push-pull test; and (b) CO_2 leakage scenarios through P&A wells into the regional aquifer at the CO_2-EOR site.

Figure S3. Illustration of P&A wells (orange symbols) where CO_2 leakage can be detected by the monitoring well (blue cross) at different times. (The gray symbols represent the P&A wells

where CO_2 leakage cannot be detected by the monitoring well.) Efficiency of the monitoring well is equal to 4/151=0.026 by 4 years, 48/151=0.073 by 15 years, and 58/151=0.099 by 35 years.

Figure S4. Piper diagram of groundwater chemistry based on groundwater samples collected from 2008 to 2014 in the shallow aquifer at the CO_2-EOR site.

Figure S5. Plot of HCO_3^- versus SiO_2 for groundwater chemistry data based on groundwater samples collected from 2008 to 2014 in the shallow aquifer at the CO_2-EOR site. A ratio of bicarbonate to silica greater than 10 suggests that groundwater chemistry is dominated mainly by carbonate mineral weathering, while a ratio less than 5 indicates that groundwater chemistry is dominated by silicate mineral weathering.[1] Groundwater chemistry data in the shallow aquifer show that ratios of bicarbonate to silicate are less than 5.

Figure S6. Plots of time evolutions of measurements of (a) alkalinity, and (b) Mn after CO_2 gas was introduced into flasks with adding aquifer sediments (orange circles) and without (blue triangles). Lines indicate results with the geochemical model.

Figure S7. Responses, simulated over time with RSRTM at a monitoring well, of (a) DIC, (b) dissolved CO_2, (c) alkalinity, and (d) pH to CO_2 leakage through a P&A well located 670 m upstream of the monitoring well, with CO_2 leakage rate ranging from 0.94 t/yr to 100.5 t/yr. Bars shown in the plots represent statistics (quartiles) of DIC, dissolved CO_2, alkalinity, and pH measured (or estimated) from 2008 through 2014 at each of 13 groundwater wells (shown in the top X-axis), and indicate the background or natural variability of the wells in the shallow aquifer. The gray crosses represent outliers.

Figure S8. Responses, simulated over time with RSRTM at a monitoring well, of (a) DIC, (b) dissolved CO_2, (c) alkalinity, and (d) pH to CO_2 leakage at five monitoring wells with different distances (6.1 km for D1, 3.6 km for D2, 1 km for D3, 0.67 km for D4, 0.3 km for D5, and 0.07 km for D6) downstream from the P&A well through which CO_2 is leaked. Bars shown in the plots represent statistics (quartiles) of DIC, dissolved CO_2, alkalinity, and pH measured (or estimated) from 2008 through 2014 at each of 13 groundwater wells (shown in the top X-axis), and indicate the background or natural variability of the wells in the shallow aquifer. The gray crosses represent outliers.

Figure S9. Detection probability (=A/S) of CO_2 leakage through a P&A well (blue dot) by a monitoring well randomly located within the CO_2-EOR site (rectangle with dash lines). Gray circles represent P&A wells, and gray triangles represent existing groundwater wells. S is the area of the CO_2-EOR site; A is the area of the CO_2 plume (dark yellow) where change in DIC, pH, dissolved CO_2, or alkalinity simulated in the model is higher than one standard of the groundwater-chemistry data collected in the shallow aquifer from 2008 through 2014.

Figure S10. Spatial distribution of detection probability of CO_2 leakage from 151 P&A wells by (a) 15 years, and (b) 50 years.

Figure S11. Plots of average detection probabilities of a CO_2 plume from 151 P&A wells over time with different (a) groundwater hydraulic gradient, and (b) CO_2 leakage rate. Bar lines represent ± one standard deviation of detection probability.

Figure S12. Illustration of P&A wells (orange symbols) where CO_2 leakage can be detected with dissolved CO_2 in groundwater by two monitoring networks: (a) GMN1 with existing groundwater wells, and (b) GMN8 with 35 groundwater wells at different times. Blue crosses represent monitoring wells; gray symbols are P&A wells where CO_2 leakage cannot be detected by the monitoring well. Configuration of the numerical simulations is the same as the run of J2 listed in Table S5. GMN1, with 13 existing groundwater wells, can detect CO_2 leakage from 20 P&A wells (ME=0.13) by 4 years, 50 P&A wells (ME=0.33) by 15 years, and 58 P&A wells (ME=0.38) by 35 years. GMN8 can detect CO_2 leakage from 62 P&A wells (ME=0.41) by 4 years, 140 P&A wells (ME=0.93) by 15 years, and 150 P&A wells (ME=0.99) by 35 years.

S2: Supplementary tables

Table S1. Reactions simulated in the geochemical model.

Table S2. Water chemistry of initial water used in batch background water and injected water used in numerical models.

Table S3. Concentration measurements of major and trace elements in shallow groundwater at CO_2-EOR site from 2008 through 2014.

Table S4. Model parameters in geochemical model of batch experiment and reactive transport model of single-well push-pull test.

Table S5. Model parameters for numerical simulations with single leakage location.

S3: Impacts of dispersion coefficient, groundwater flow direction, and aquifer heterogeneity on monitoring efficiency of a monitoring network at the CO_2-EOR site

Figure S13. Comparison of monitoring efficiency with (a) GMN1, and (b) GMN7 for dissolved CO_2, with different longitudinal dispersion coefficients, α_L. (Note that the ratio of the longitudinal dispersion coefficient to the transverse dispersion coefficient keeps constant, 2 for the three runs.)

Figure S14. Comparison of monitoring efficiency of (a) GMN1, and (b) GMN7, with dissolved CO_2 for different groundwater-flow directions in the numerical simulations (Table S5).

Figure S15. Spatial distribution of hypothetic hydraulic conductivity field (m/day) used in the numerical simulation to consider impacts of aquifer heterogeneity on the monitoring efficiency of the nine monitoring networks shown in Figure 1. Note that the hydraulic field in the simulation run does not necessarily represent the real hydraulic conductivity in the regional aquifer of the study area.

Figure S16. Comparison of monitoring efficiency with (a) GMN1, (b) GMN3, and (c) GMN9 for dissolved CO_2 in homogeneous and heterogeneous aquifers. (Distribution of hydraulic conductivity is shown in Figure S15.)

S1. Supplementary Figures

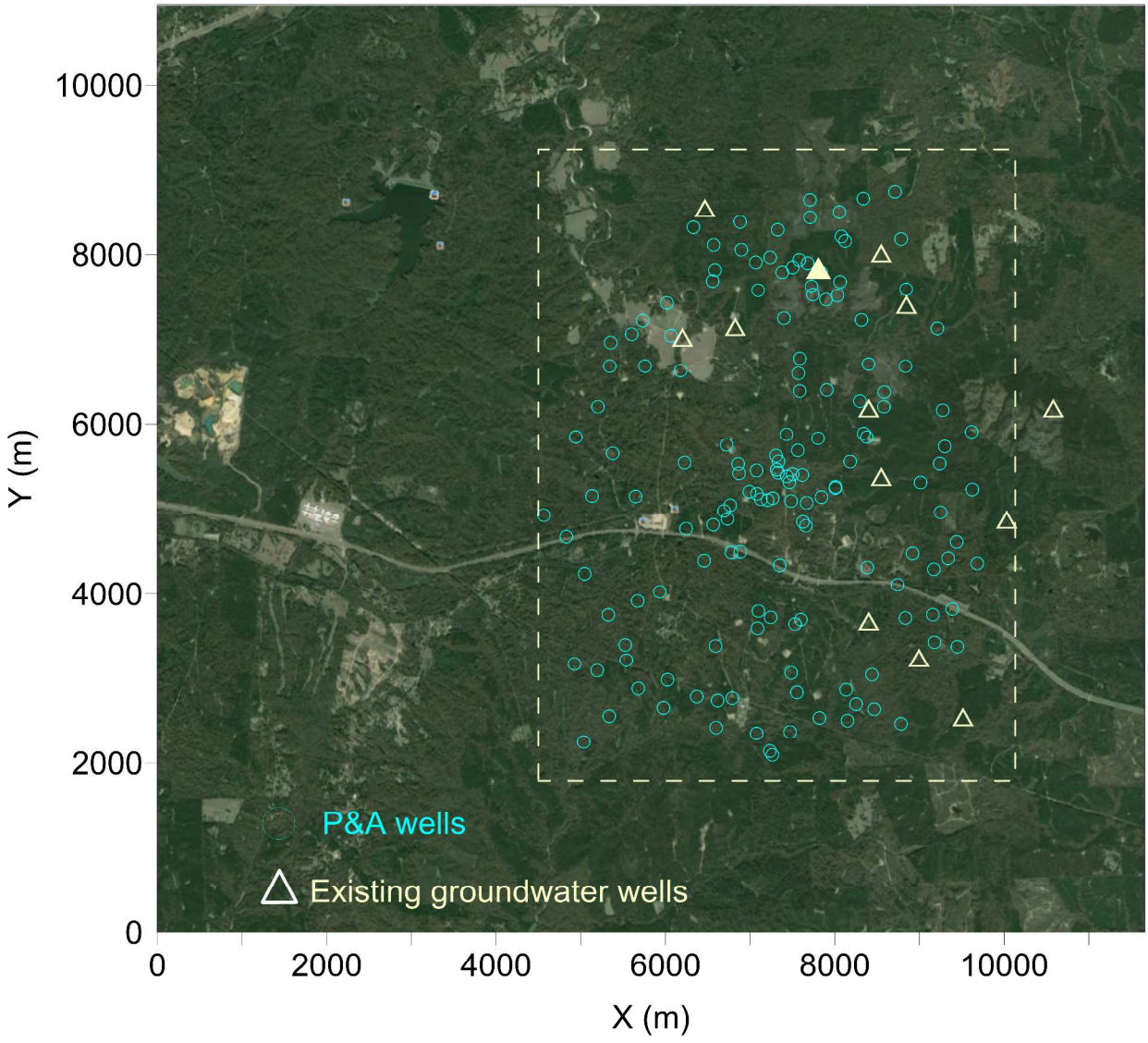

Figure S1. Plot of the CO_2–EOR site, the Cranfield oil and gas field, located at about 25 km east of the city of Natchez, Adams County, Mississippi. In the plot, circles are plugged and abandoned (P&A) wells and triangles represent existing groundwater wells in the shallow aquifer. The rectangle with dash lines represents the approximate location of the CO_2-EOR site and the solid

triangle represents the monitoring well (UM-1) drilled into the sand unit of the Catahoula Formation and cored for aquifer sediments, as well as for the push-pull test.

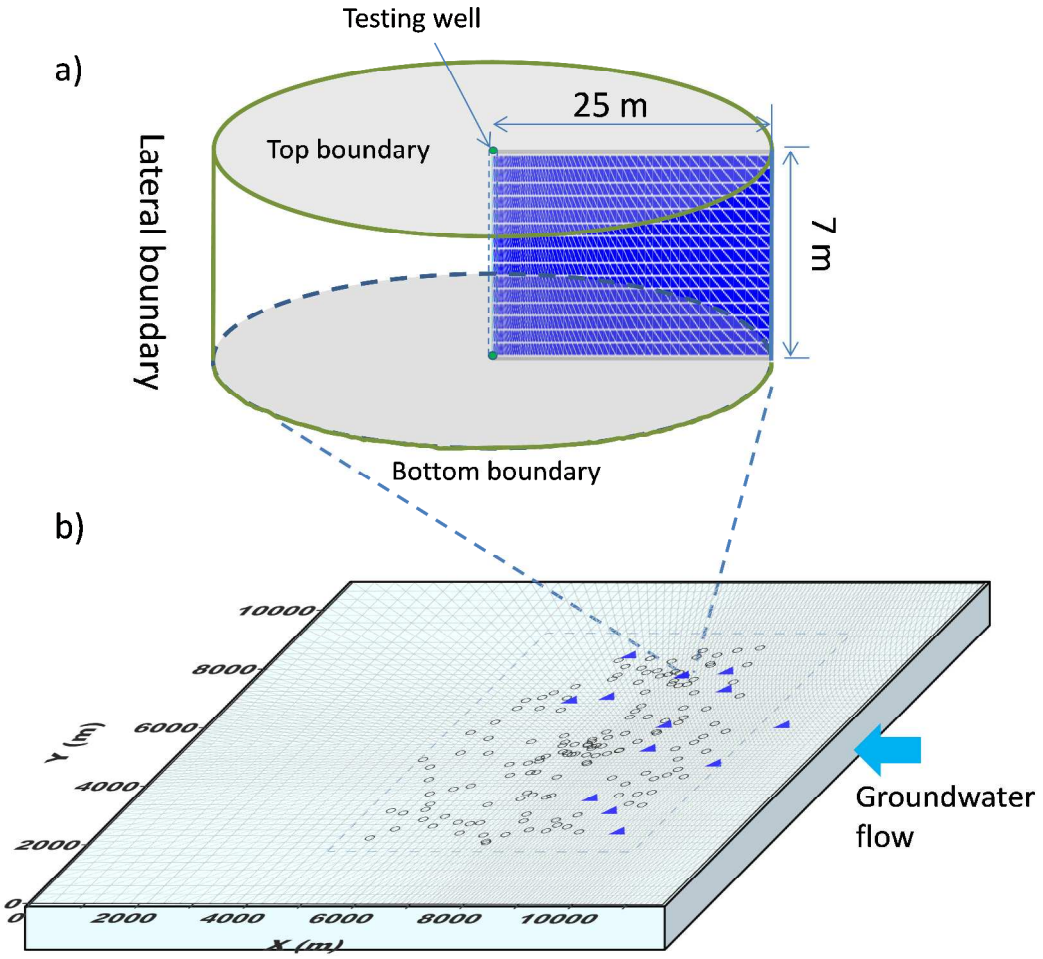

Figure S2. Model domain for reactive transport modeling (RTM) of (a) the single-well push-pull test; and (b) CO_2 leakage scenarios through P&A wells into the regional aquifer at the CO_2-EOR site.

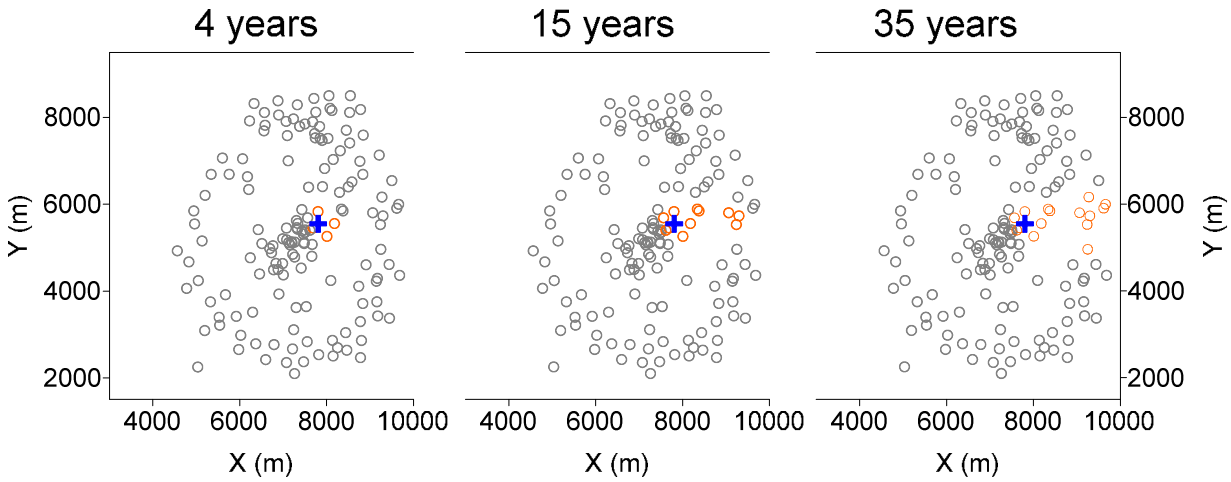

Figure S3. Illustration of P&A wells (orange symbols) where CO_2 leakage can be detected by the monitoring well (blue cross) at different times. (The gray symbols represent the P&A wells where CO_2 leakage cannot be detected by the monitoring well.) Efficiency of the monitoring well is equal to 4/151=0.026 by 4 years, 48/151=0.073 by 15 years, and 58/151=0.099 by 35 years.

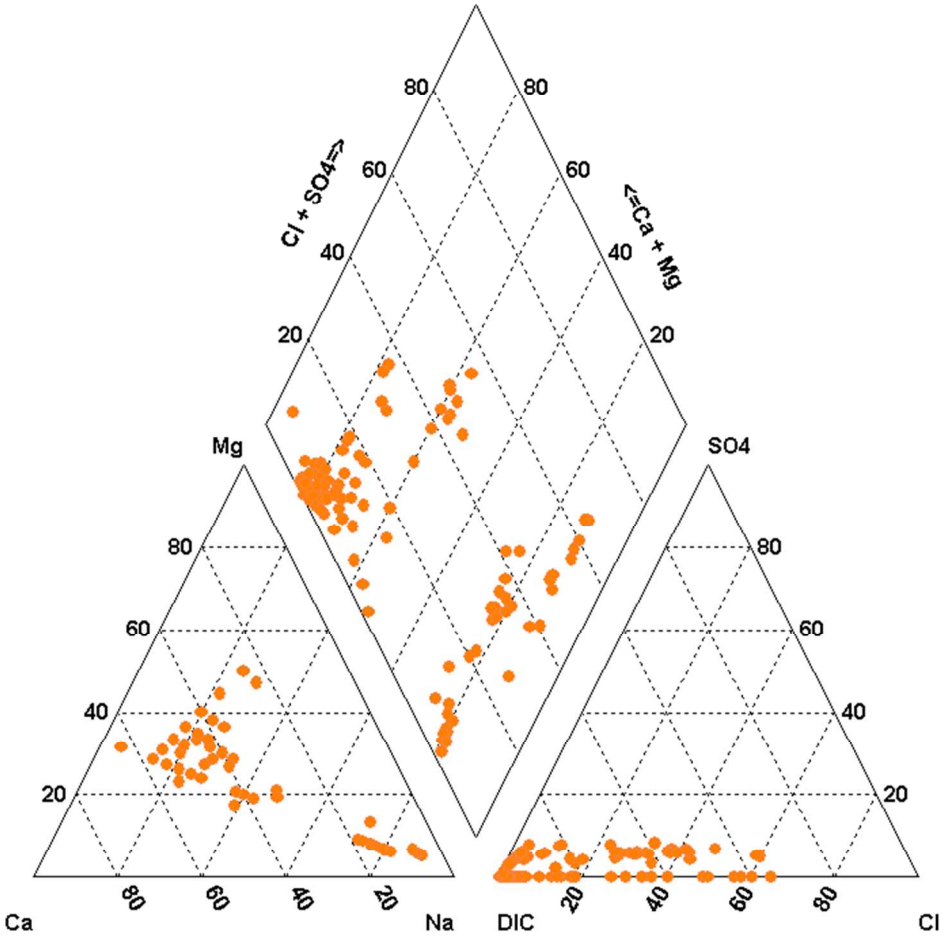

Figure S4. Piper diagram of groundwater chemistry based on groundwater samples collected from 2008 to 2014 in the shallow aquifer at the CO_2-EOR site.

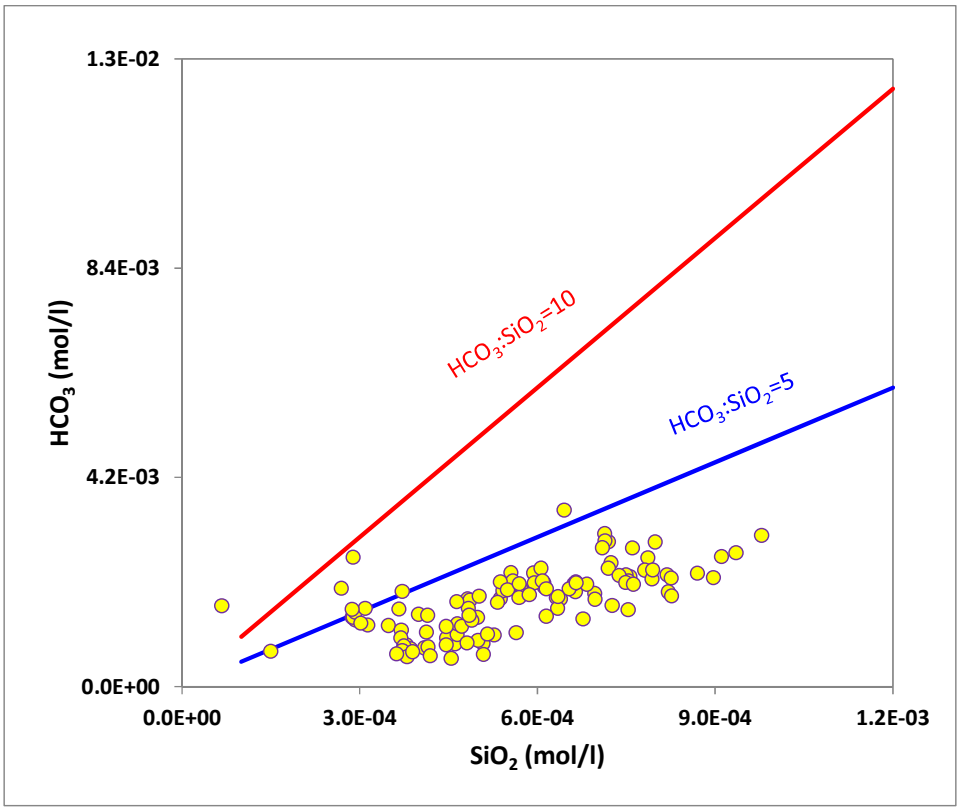

Figure S5. Plot of HCO_3^- versus SiO_2 for groundwater chemistry data based on groundwater samples collected from 2008 to 2014 in the shallow aquifer at the CO_2-EOR site. A ratio of bicarbonate to silica greater than 10 suggests that groundwater chemistry is dominated mainly by carbonate mineral weathering, while a ratio less than 5 indicates that groundwater chemistry is dominated by silicate mineral weathering.[1] Groundwater chemistry data in the shallow aquifer show that ratios of bicarbonate to silicate are less than 5.

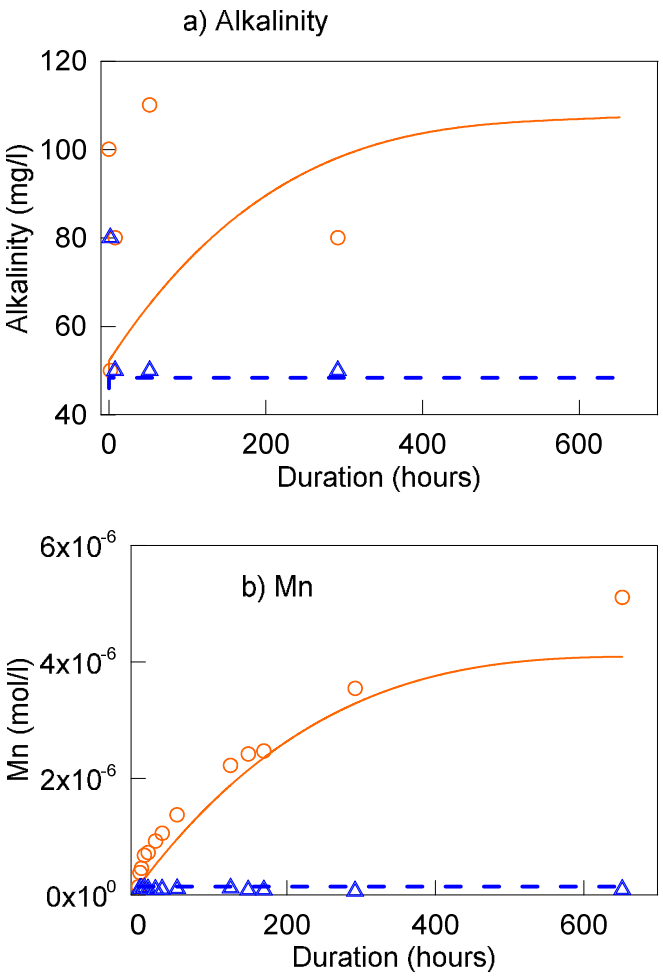

Figure S6. Plots of time evolutions of measurements of (a) alkalinity, and (b) Mn after CO_2 gas was introduced into flasks with adding aquifer sediments (orange circles) and without (blue triangles). Lines indicate results with the geochemical model.

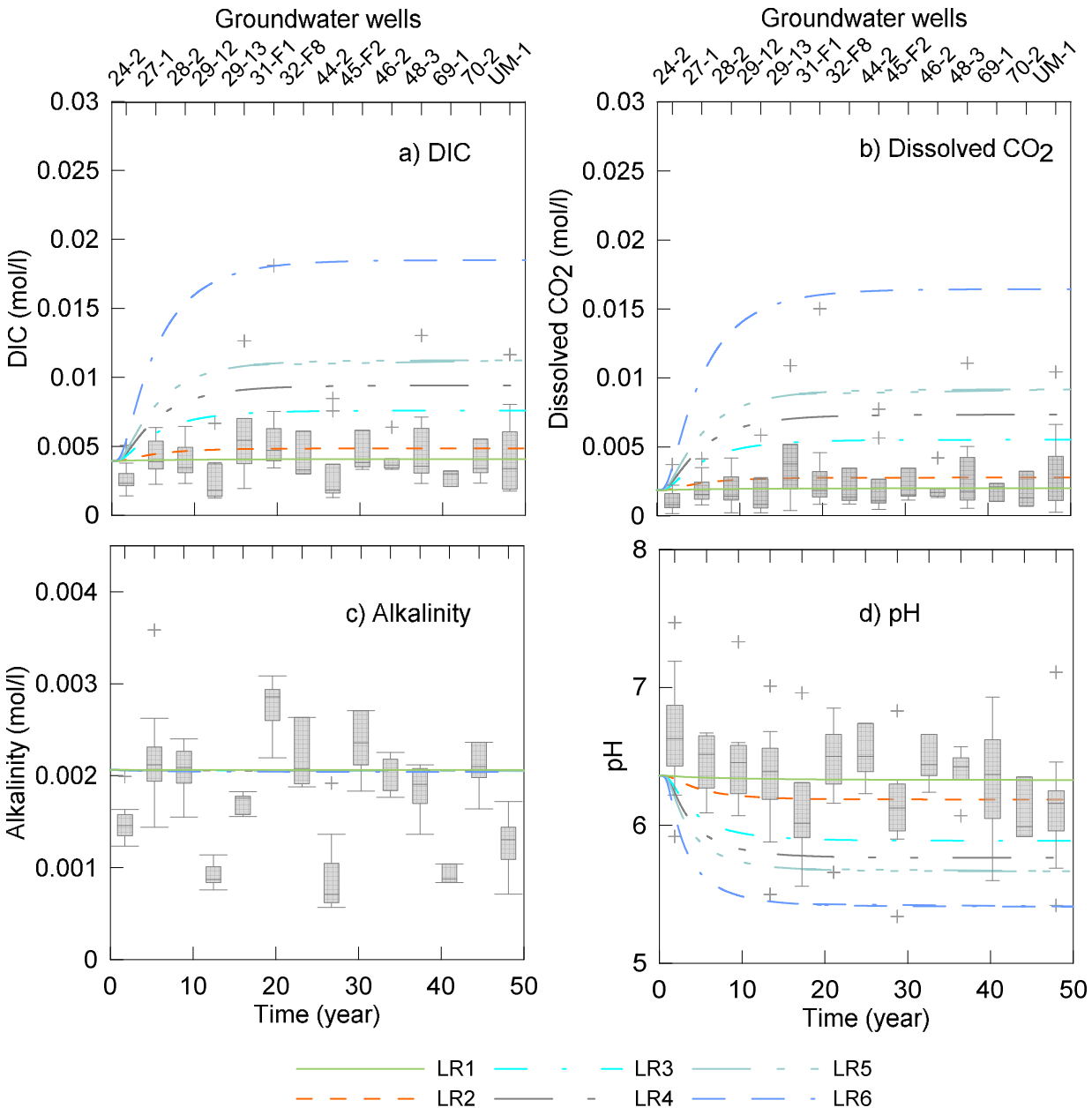

Figure S7. Responses, simulated over time with RSRTM at a monitoring well, of (a) DIC, (b) dissolved CO_2, (c) alkalinity, and (d) pH to CO_2 leakage through a P&A well located 670 m upstream of the monitoring well, with CO_2 leakage rate ranging from 0.94 t/yr to 100.5 t/yr. Bars shown in the plots represent statistics (quartiles) of DIC, dissolved CO_2, alkalinity, and pH measured (or estimated) from 2008 through 2014 at each of 13 groundwater wells (shown in the top X-axis), and indicate the background or natural variability of the wells in the shallow aquifer. The gray crosses represent outliers.

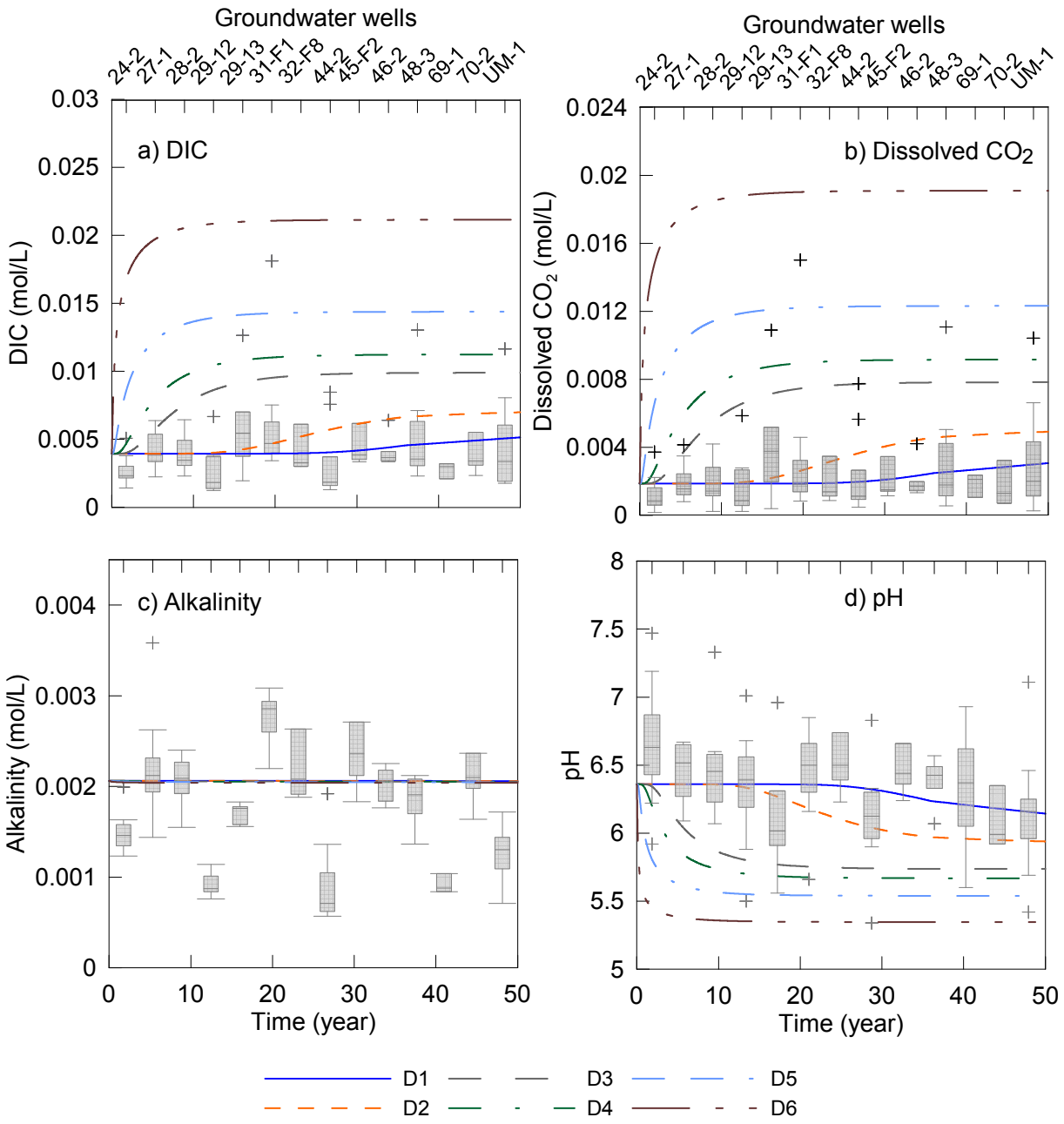

Figure S8. Responses, simulated over time with RSRTM at a monitoring well, of (a) DIC, (b) dissolved CO_2, (c) alkalinity, and (d) pH to CO_2 leakage at five monitoring wells with different distances (6.1 km for D1, 3.6 km for D2, 1 km for D3, 0.67 km for D4, 0.3 km for D5, and 0.07 km for D6) downstream from the P&A well through which CO_2 is leaked. Bars shown in the plots represent statistics (quartiles) of DIC, dissolved CO_2, alkalinity, and pH measured (or estimated) from 2008 through 2014 at each of 13 groundwater wells (shown in the top X-axis), and indicate the background or natural variability of the wells in the shallow aquifer. The gray crosses represent outliers.

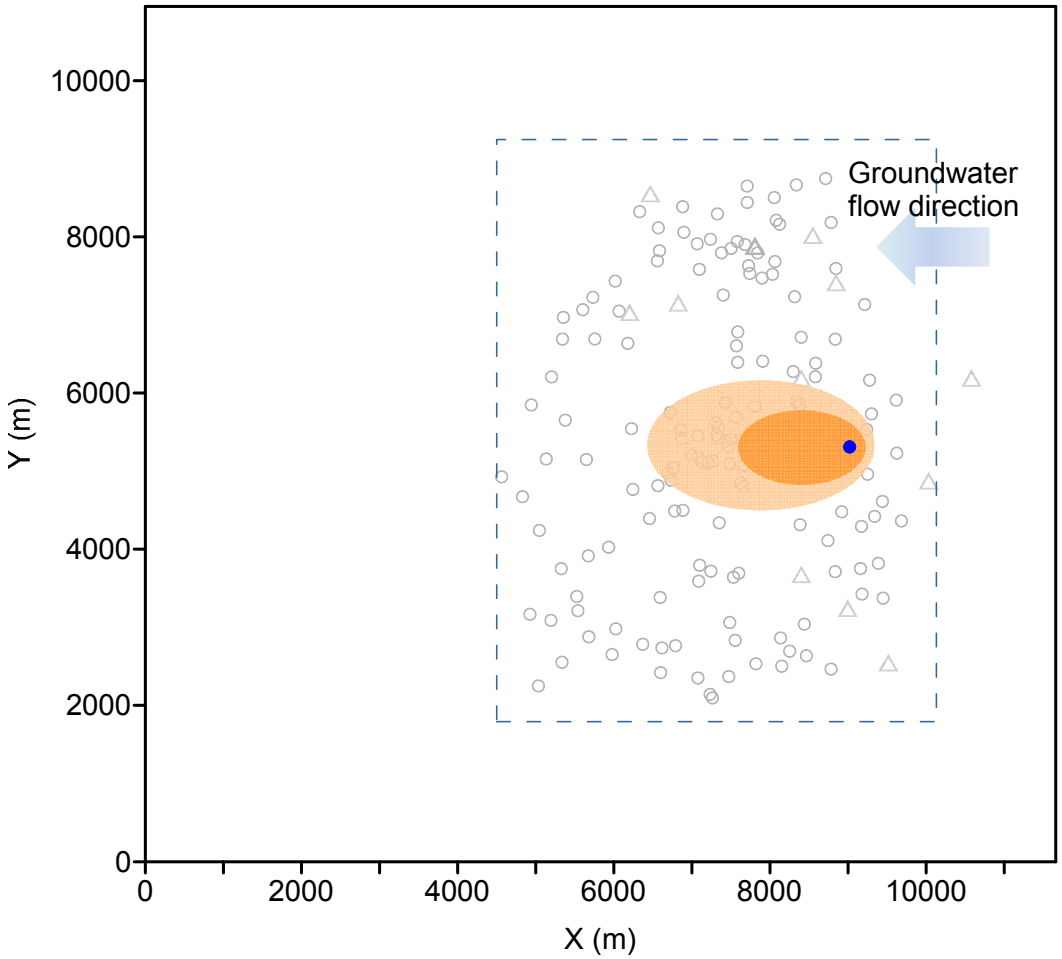

Figure S9. Detection probability (=A/S) of CO_2 leakage through a P&A well (blue dot) by a monitoring well randomly located within the CO_2-EOR site (rectangle with dash lines). Gray circles represent P&A wells, and gray triangles represent existing groundwater wells. S is the area of the CO_2-EOR site; A is the area of the CO_2 plume (dark yellow) where change in DIC, pH, dissolved CO_2, or alkalinity simulated in the model is higher than one standard of the groundwater-chemistry data collected in the shallow aquifer from 2008 through 2014.

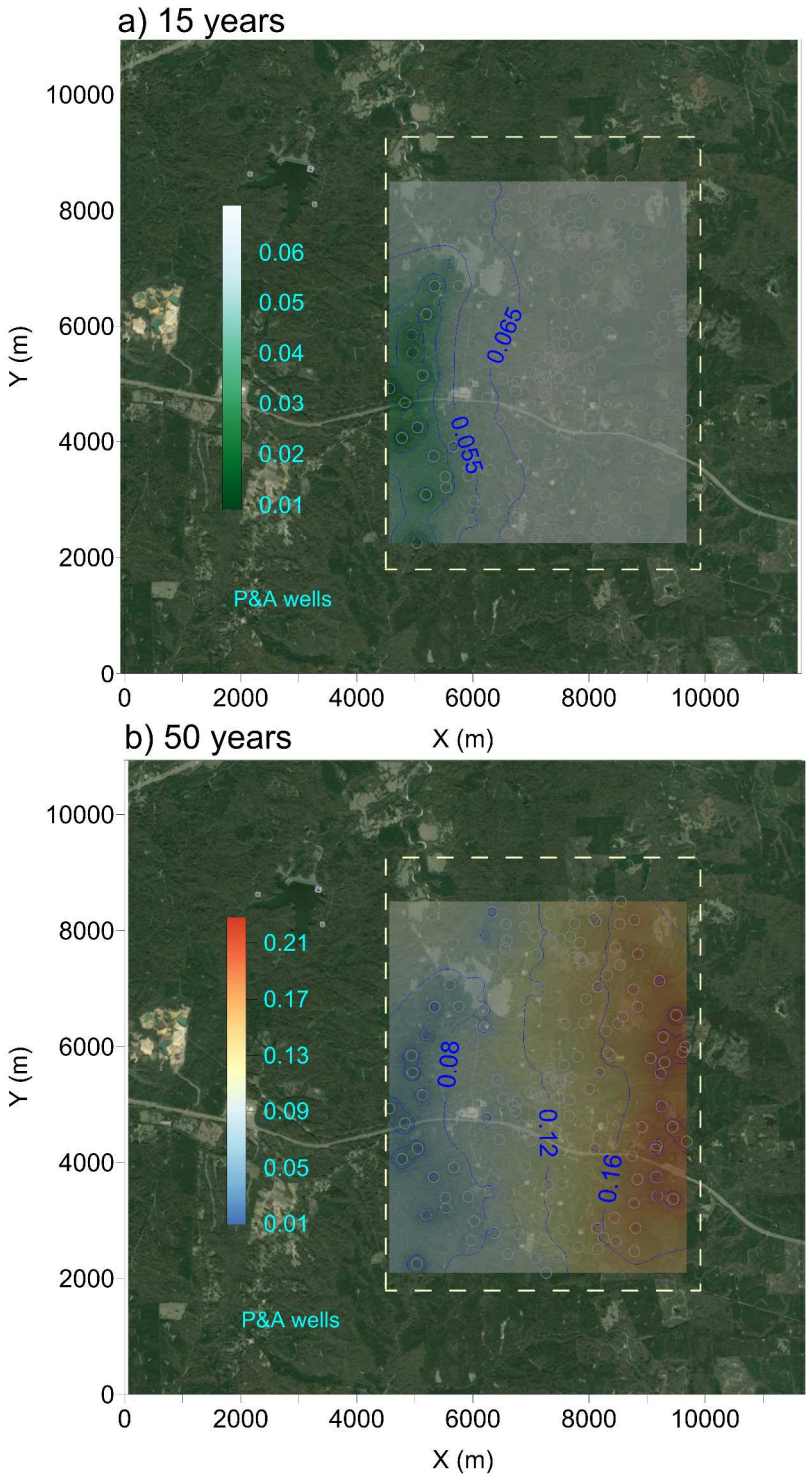

Figure S10. Spatial distribution of detection probability of CO_2 leakage from 151 P&A wells by (a) 15 years, and (b) 50 years.

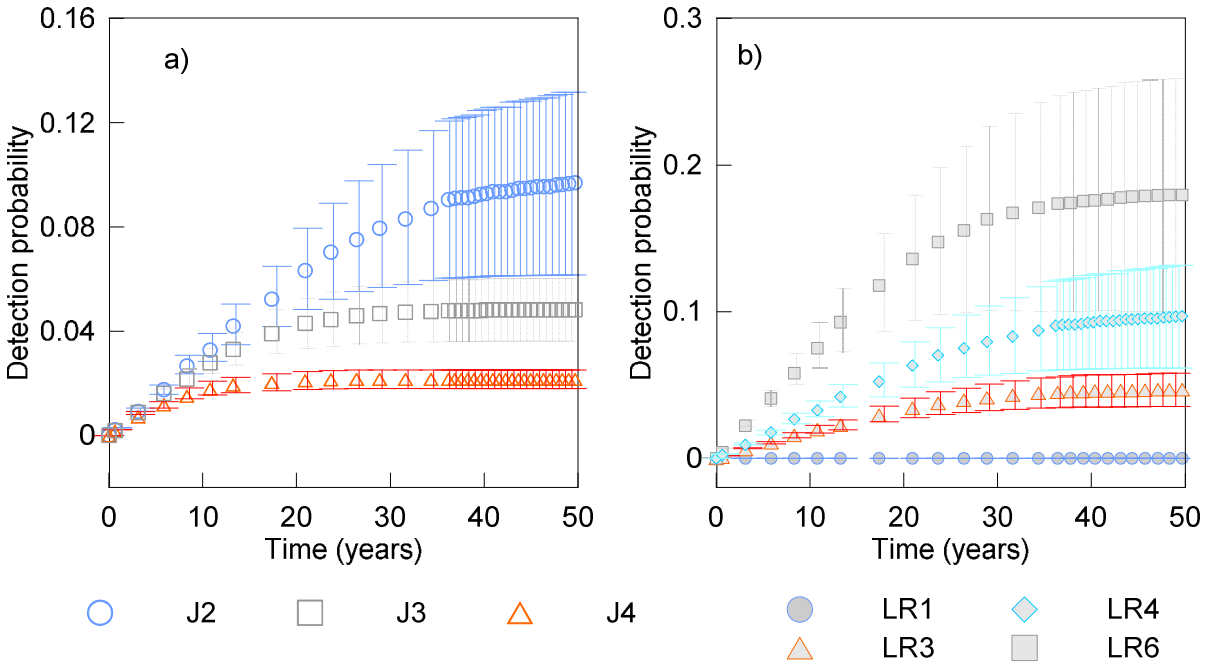

Figure S11. Plots of average detection probabilities of a CO_2 plume from 151 P&A wells over time with different (a) groundwater hydraulic gradient, and (b) CO_2 leakage rate. Bar lines represent ± one standard deviation of detection probability.

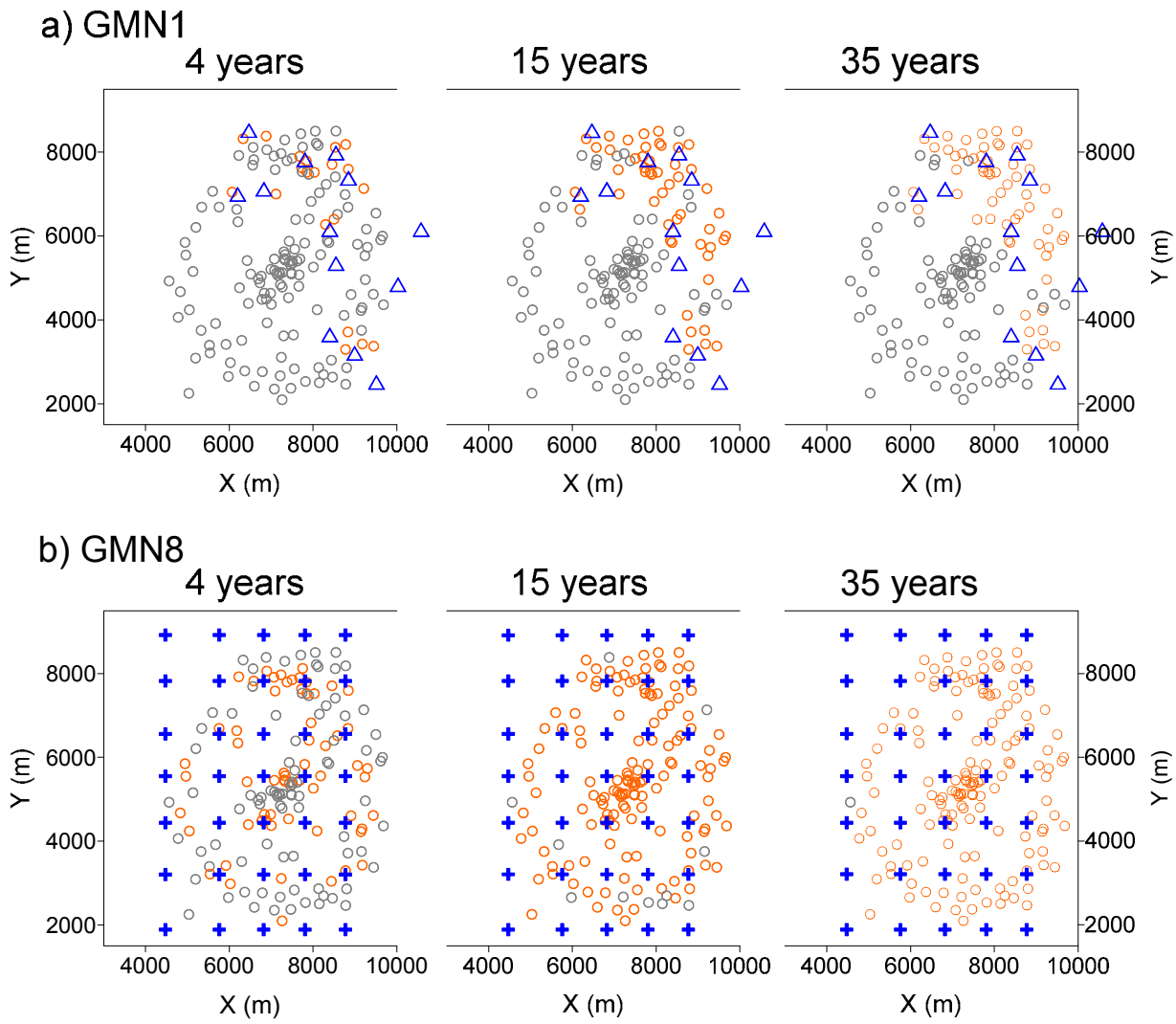

Figure S12. Illustration of P&A wells (orange symbols) where CO_2 leakage can be detected with dissolved CO_2 in groundwater by two monitoring networks: (a) GMN1 with existing groundwater wells, and (b) GMN8 with 35 groundwater wells at different times. Blue crosses represent monitoring wells; gray symbols are P&A wells where CO_2 leakage cannot be detected by the monitoring well. Configuration of the numerical simulations is the same as the run of J2 listed in Table S5. GMN1, with 13 existing groundwater wells, can detect CO_2 leakage from 20 P&A wells (ME=0.13) by 4 years, 50 P&A wells (ME=0.33) by 15 years, and 58 P&A wells (ME=0.38) by 35 years. GMN8 can detect CO_2 leakage from 62 P&A wells (ME=0.41) by 4 years, 140 P&A wells (ME=0.93) by 15 years, and 150 P&A wells (ME=0.99) by 35 years.

S2. Supplementary Tables

Table S1. Reactions simulated in the geochemical model

Aqueous complexes and their dissociation constants

Aqueous complex	$Log_{10}K$ (25°C)	Aqueous complex	$Log_{10}K$ (25°C)	Aqueous complex	$Log_{10}K$ (25°C)	Aqueous complex	$Log_{10}K$ (25°C)	Aqueous complex	$Log_{10}K$ (25°C)
$Al(oh)_2^+$	10.10	$H_2AsO_4^-$	-21.41	$NaCO_3^-$	9.81	$BaCl^+$	0.50	$HSiO_3^-$	9.95
$Al(oh)_{3(aq)}$	16.16	$H_3AsO4(aq)$	-23.64	$NaSO_4^-$	-0.82	$BaOH^+$	13.47	HSO_4^-	-1.98
$Al(oh)_4^-$	22.15	$HAsO_4^{2-}$	-14.66	$PbOH^+$	7.57	$CaCl^+$	0.70	$KBr_{(aq)}$	1.74
$Pb(OH)_{2(aq)}$	17.07	$CaHCO_3^+$	-1.05	$KCl_{(aq)}$	1.50	$PbCO_{3(aq)}$	-3.06	$CuCl^+$	-0.44
$Pb\ (CO_3)_2^{2-}$	11.24	$CaOH^+$	12.85	$KOH_{(aq)}$	14.46	$PbCl^+$	-.45	$FeCl^+$	0.17
$PbHCO_3^+$	-2.89	$CaSO_{4(aq)}$	-2.11	KSO_4^-	-0.88	$PbCl_{2(aq)}$	-2.01	$FeHCO_3^+$	-2.04
$MgCl^+$	0.14	$PbCl_3^-$	-1.70	$H_2AsO_3^-$	9.13	$MnCl^+$	-0.30	$CO_{2(aq)}$	-6.34
$MgCO_{3(aq)}$	7.35	$PbCl_4^{2-}$	−1.50	$H_3AsO_4(aq)$	-23.64	$NaBr_{(aq)}$	1.36	CO_3^{2-}	10.33
$MgHCO_3^+$	-1.04	OH^-	13.99	$H_2AsO_4^-$	-21.41	$NaCl_{(aq)}$	0.78		

Mineral reactions and kinetic parameters[a]

Mineral	$Log_{10}K$	Neutral mechanism		Acid mechanism			Base mechanism		
		k (mol/m²/s)	E(kj/mol)	k (mol/m²/s)	E(kj/mol)	n_1	k(mol/m²/s)	E(kj/mol)	n_3
Quartz	-4.00	3.023×10^{-14}	87.7						
Kaolinite	5.10	6.918×10^{-14}	22.2	4.898×10^{-14}	65.9	0.78	8.913×10^{-18}	17.9	-0.472
Dolomite	2.51	2.951×10^{-8}	52.2	6.464×10^{-4}	36.1	0.5	7.762×10^{-6}	34.8	0.5[b]
Illite	7.06	1.660×10^{-13}	35	1.047×10^{-11}	23.6	0.34	3.020×10^{-17}	58.9	-0.4
K-feldspar	-1.13	3.890×10^{-13}	38	8.710×10^{-11}	51.7	0.5	6.310×10^{-22}	94.1	-0.823
Albite	1.91	2.754×10^{-13}	69.8	6.918×10^{-11}	65.0	0.46	2.512×10^{-16}	71	-0.572

Surface complex of arsenic and lead on kaolinite and illite

Adsorbent	Surface complexes	Reactions	Log K_{int}
Kaolinite	Kao_Pb+	$Kao\_OPb^+ + H^+ \rightleftharpoons Kao\_OH + Pb^{2+}$	-1.89[c]
	$Kao\_H_2ASO_3$	$Kao\_H_2ASO_3 + H_2O \rightleftharpoons Kao\_OH + H_3ASO_3$	-8.23[d]
	$Kao\_HASO_3^-$	$Kao\_HASO_3^- + H_2O + H^+ \rightleftharpoons Kao\_OH + H_3ASO_3$	0.664[e]
	$Kao\_ASO_3^{2-}$	$Kao\_HASO_3^{2-} + H_2O + H^+ \rightleftharpoons Kao\_OH + H_3ASO_3$	13.67[e]
Illite	Ill^s_OPB+	$Ill^s\_OPb^+ + H^+ \rightleftharpoons Ill^s\_O + Pb^{2+}$	-1.37[f]
	Ill^w_OPB+	$Ill^w\_OPb^+ + H^+ \rightleftharpoons Illw\_O + Pb^{2+}$	3.84[f]
	$Ill\_H_2ASO_3$	$Ill\_H_2ASO_3 + H_2O \rightleftharpoons Ill\_OH + H_3ASO_3$	-9.07[g]
	Ill_HASO_3	$Ill\_HASO_3^- + H_2O + H^+ \rightleftharpoons Ill\_OH + H_3ASO_3$	-3.0[g]
	$Ill\_ASO_3^{2-}$	$Ill\_HASO_3^{2-} + H_2O + H^+ \rightleftharpoons Ill\_OH + H_3ASO_3$	10.3[g]

Cation exchange reactions and selectivity coefficients[h]

Cation exchange reaction	$K_{Na/M}$	Cation exchange reaction	$K_{Na/M}$
$Na^+ + X–K \leftrightarrow X–Na + K^+$	0.2	$Na^+ + 0.5\ X–Ca \leftrightarrow X–Na + 0.5\ Ca^{2+}$	0.4
$Na^+ + 0.5\ X–Mg \leftrightarrow X–Na + 0.5\ Mg^{2+}$	0.45	$Na^+ + 0.5\ X–Mn \leftrightarrow X–Na + 0.5\ Mn^{2+}$	0.55
$Na^+ + 0.5\ X–Ba \leftrightarrow X–Na + 0.5\ Ba^{2+}$	0.35		

Note:

[a] All rate constants are listed for dissolution and rate laws that can be described by

$$\frac{dm}{dt} = -S_A \begin{bmatrix} k_{acid}^{298.15\,K} e^{\frac{-E_{acid}}{R}\left(\frac{1}{T}-\frac{1}{298.15K}\right)} a_{H^+}^{n_1}(1-\Omega^{p_1})^{q_1} \\ +k_{Neut}^{298.15\,K} e^{\frac{-E_{neut}}{R}\left(\frac{1}{T}-\frac{1}{298.15K}\right)}(1-\Omega^{p_2})^{q_2} \\ +k_{base}^{298.15\,K} e^{\frac{-E_{base}}{R}\left(\frac{1}{T}-\frac{1}{298.15K}\right)} a_{H^+}^{n_3}(1-\Omega^{p_3})^{q_3} \end{bmatrix}$$

where S_A is reactive surface area; $k_{acid}^{298.15}$, $k_{neutral}^{298.15}$, $k_{base}^{298.15}$ are rate constants for acid, neutral, and base conditions, respectively, at a temperature of 298.15 K; E_{acid}, E_{neut}, E_{base} are activation energies (J mol^{-1}); T is temperature (K); R is gas constant; Ω is mineral saturation index; p and q are empirical and dimensionless parameters; a_{H+} is activity of H^+ in water; and n is reaction order.

[b] Reaction order of n_3 with respect to $P(CO_2)$.

[c] K_{int} from Müller and Sigg, 1992.

[d] K_{int} from Manning and Goldberg, 1997.

[e] K_{int} from Gu and Evans, 2007.

[f] K_{int} from Manning and Goldberg, 1997.

[g] Selectivity coefficients from Appelo and Postma, 2005.

Table S2. Water chemistry of initial water used in batch background water and injected water used in numerical models

Species	Batch-scale model for lab experiment [a] (M)	Site-scale model for push-pull test		Regional scale model	
		Background water [b] (M)	Injected water [c] (M)	Background water [d] (M)	Leakage water [e] (M)
Al	2.28×10^{-6}	4.52×10^{-8}	4.53×10^{-8}	6.94×10^{-8}	6.94×10^{-8}
As	2.67×10^{-9}	2.67×10^{-9}	2.68×10^{-9}	2.04×10^{-9}	2.04×10^{-9}
Ba	6.01×10^{-7}	5.05×10^{-7}	5.06×10^{-7}	8.83×10^{-7}	8.83×10^{-7} ($5.48\times10^{-4)}$
Br	8.76×10^{-7}	1.25×10^{-7}	1.43×10^{-3}	8.43×10^{-7}	8.43×10^{-7}
Ca	5.28×10^{-4}	4.70×10^{-4}	4.90×10^{-4}	3.92×10^{-4}	3.92×10^{-4} ($3.01\times10^{-1)}$
Cd	3.56×10^{-10}	1.62×10^{-9}	1.61×10^{-9}	8.07×10^{-9}	8.07×10^{-9} (5.22×10^{-7})
Cl	2.95×10^{-4}	7.36×10^{-4}	7.38×10^{-4}	6.08×10^{-4}	6.08×10^{-4} (2.935×10^{-0})
Cu	3.94×10^{-8}	1.24×10^{-8}	1.25×10^{-8}	7.28×10^{-8}	7.28×10^{-8}
Fe	5.45×10^{-6}	3.21×10^{-8}	3.21×10^{-8}	3.12×10^{-5}	3.12×10^{-5} (3.20×10^{-8})
K	1.31×10^{-4}	3.45×10^{-5}	3.49×10^{-5}	6.96×10^{-5}	6.96×10^{-5}
Mg	3.46×10^{-4}	3.31×10^{-4}	3.39×10^{-4}	2.63×10^{-4}	2.63×10^{-4} (4.55×10^{-2})
Mn	1.41×10^{-7}	2.60×10^{-8}	2.61×10^{-8}	3.16×10^{-6}	3.16×10^{-6} (3.84×10^{-4})
Na	6.25×10^{-4}	5.04×10^{-4}	1.85×10^{-3}	1.09×10^{-3}	1.09×10^{-3} (2.23×10^{-0})
Pb	1.45×10^{-10}	1.45×10^{-10}	1.25×10^{-10}	5.47×10^{-9}	5.47×10^{-9} (3.04×10^{-6})
Si	4.50×10^{-4}	4.72×10^{-4}	4.80×10^{-4}	5.34×10^{-4}	5.34×10^{-4} (4.72×10^{-4})
SO4	1.06×10^{-4}	8.27E-07	9.71×10^{-6}	3.03×10^{-5}	3.03×10^{-5} (5.07×10^{-7})
Dissolved inorganic carbon	2.00×10^{-3}	3.81×10^{-3}	3.53×10^{-2}	3.94×10^{-3}	0.362
pH	8.57	5.8	4.9	6.36	3.7

Notes:

[a] Water chemistry in the flask prior to CO_2 bubbling, used as an initial condition in the geochemical model for the batch experiment.

[b] Water chemistry in the shallow aquifer before the push-pull test was conducted, used as an initial condition in the reactive transport model for the push-pull test.

[c] Water chemistry injected into the shallow aquifer.

[d] Water chemistry averaged based on groundwater chemistry data during the period of 2008 to 2014.

[e] Groundwater chemistry obtained by equilibrating background water chemistry with CO_2 gas at pressure of 4 atm using PHREEQC[2]. The values within the parentheses for the brine compositions are from Lu et al. (2012)[3]

Table S3. Concentration measurements of major and trace elements in shallow groundwater at CO_2-EOR site from 2008 through 2014

	T (°C)	Conductivity uS/cm[2]	pH	Alkalinity mg $CaCO_3$/ l	Dissolved inorganic carbon[b] (mmol/l)	Ca ppm	Mg ppm	K ppm	Na ppm	Si ppm	Cl ppm	SO4 ppm
EPA MCL[c]			6.5-8.5[a]							1.9	250[a]	250[a]
Minimum	17.6	111.6	5.34	30	1.2	3.9	1.5	1.1	7.6	1.9	2.7	0.2
Q1	20.2	217.0	6.16	61	2.3	8.4	2.3	1.5	9.6	11.6	4.8	3.9
Q2	20.9	232.5	6.38	89	3.4	20.0	8.1	2.0	12.1	15.6	5.8	4.9
Q3	21.5	263.5	6.58	107	4.6	23.0	9.0	2.8	31.6	19.6	37.0	8.4
Maximum	25.8	391.1	7.47	154	18.1	27.9	10.2	8.4	74.3	27.5	95.1	13.7
stdev	1.3	53.8	0.4	31.9	2.5	7.5	3.1	1.9	19.1	5.2	25.5	3.0

	Al (ppb)	As ppb	Ba ppb	Cd ppb	Cr ppb	Cu ppb	Fe ppm	Mn ppb	Pb ppb	Zn ppb
EPA MCL	50-200[a]	10	2000	5	100	1000[a]	0.3[a]	50[a]	15	5000[a]
Minimum	0.01	0.11	6.8	0.0	0.027	0.043	0.001	0.6	9.3×10^{-4}	0.5
Q1	1.09	0.54	35.5	0.4	0.093	0.52	0.044	9	0.014	7.3
Q2	1.21	0.74	130.3	1.0	0.26	3.0	0.7	107	0.036	16.2
Q3	1.46	1.62	190.0	3.0	2.0	6.9	1.8	168	7.7	23.8
Maximum	17.6	33	271.8	5.9	3.0	34	14.9	708	12.0	1187
stdev	4.0	8.3	79.5	1.7	1.1	6.2	3.3	179	4.34	214.4

Notes:

[a] Secondary maximum contamination level in national secondary drinking-water regulation.

[b]. Dissolved inorganic carbon (DIC) of each groundwater sample was estimated based on groundwater chemistry using PHREEQC.

[c] EPA MCL represents maximum contamination level regulated by US EPA primary and secondary drinking water standards.

Q1 is the middle number between the minimum and the median of the data set; *Q2* is the median of the data set; *Q3* is the middle value between the median and maximum value of the data set; and *stdev* stands for "standard deviation of the data set."

Table S4. Model parameters in geochemical model of batch experiment and reactive transport model of single-well push-pull test

Model parameters		Batch experiment	Single-well PPT
Volume fraction in aquifer sediments	Dolomite (%)	1.45×10^{-3} (1.18×10^{-3}, 3.93×10^{-2})[a]	5.90×10^{-4} (1.0×10^{-5},2.4×10^{-2}) [a]
	Albite (%)	1.92	1.92
	K-feldspar (%)	18.18	18.18
	Kaolinite (%)	25.80	25.80
	Illite (%)	8.16	8.16
	Quartz (%)	45.94	45.94
Reactive surface area (RSA)(m^2/g)[c]	Dolomite	1.26×10^{-5} (1.24×10^{-5}, 1.28×10^{-5}) [a]	6.91×10^{-8} (4.19×10^{-10}, 3.51×10^{-7}) [a]
	Albite	4.39×10^{-2} (3.5×10^{-2}, 5.29×10^{-2})	4.4×10^{-3} (1.3×10^{-3}, 6.5×10^{-3}) [a]
	K-feldspar	5.61×10^{-2} (1.29×10^{-2}, 5.92×10^{-2}) [a]	8.35×10^{-5} (2.11×10^{-5}, 1.46×10^{-4})
	Kaolinite	3.35×10^{-3} (1.08×10^{-3}, 1.81×10^{-1}) [a]	4.18×10^{-5} (4.19×10^{-7}, 8.59×10^{-5}) [a]
	Quartz	6.13×10^{-2} (3.62×10^{-3}, 9.04×10^{-2}) [a]	3.62×10^{-2} (3.49×10^{-3}, 3.75×10^{-2}) [a]
	Illite	2.51×10^{-3} (7.23×10^{-4}, 5.42×10^{-2}) [a]	3.60×10^{-3} (3.19×10^{-4}, 4.01×10^{-2}) [a]
Total concentration of adsorbed components	Kaolinite (mol/m^2)	1.2×10^{-8} (5.85×10^{-11}, 3.43×10^{-8}) [a]	1.2×10^{-8}
	Illite_w (mol/m^2)	2.87×10^{-9} (4.05×10^{-12}, 3.15×10^{-8}) [a]	2.87×10^{-9}
	Illite_s (mol/m^2)	3.36×10^{-10} (4.75×10^{-12}, 1.06×10^{-7}) [a]	3.36×10^{-10}
Transport parameters	Hydraulic conductivity (m/day)	N/A	7.62 (7.55, 7.69) [a]
	Longitudinal dispersivity coefficient[b] (m^{-1})	N/A	1.5 (1.40, 1.60) [a]
	Porosity	N/A	0.1 (0.08, 0.13) [a]

Notes:

[a] The numbers between parentheses are the 95% confidence interval of the parameter, estimated with inverse algorithms.

[b] The transverse dispersivity coefficient is set at half of the longitudinal dispersivity coefficient.

[c] The surface area is for aquifer materials.

Table S5. Model parameters for numerical simulations with single leakage location

	Runs	K (m/day)	Hydrodynamic dispersion coefficient (m)	Porosity	Hydraulic gradient (%)	Flow direction [a]	Leakage rate[d] (Ton CO_2/year)
With and without brine	Run1	7.6	α_L=250, α_T=130	0.1	**0.5**	0°	50.3 (0.50%)
	BR1[c]	7.6	α_L=250, α_T=130	0.1	**0.5**	0°	37.7 (0.38%)
	BR2[c]	7.6	α_L=250, α_T=130	0.1	**0.5**	0°	50.3 (0.50%)
Natural gradient	J1	7.6	α_L=250, α_T=130	0.1	**0.1**	0°	37.7 (0.38%)[b]
	J2	7.6	α_L=250, α_T=130	0.1	**0.5**	0°	37.7 (0.38%)
	J3	7.6	α_L=250, α_T=130	0.1	**0.8**	0°	37.7 (0.38%)
	J4	7.6	α_L=250, α_T=130	0.1	**1.0**	0°	37.7 (0.38%)
Leakage rate	LR1	7.6	α_L=250, α_T=130	0.1	**0.5**	0°	0.943 (0.009%)
	LR2	7.6	α_L=250, α_T=130	0.1	**0.5**	0°	6.28 (0.063%)
	LR3	7.6	α_L=250, α_T=130	0.1	**0.5**	0°	25.1 (0.25%)
	LR4[e]	7.6	α_L=250, α_T=130	0.1	**0.5**	0°	37.7 (0.38%)
	LR5	7.6	α_L=250, α_T=130	0.1	**0.5**	0°	50.3 (0.50%)
	LR6	7.6	α_L=250, α_T=130	0.1	**0.5**	0°	100.5 (1.0%)
Regional flow direction	FD1	7.6	α_L=250, α_T=130	0.1	**0.5**	30°	37.7 (0.38%)
	FD2	7.6	α_L=250, α_T=130	0.1	**0.5**	45°	37.7 (0.38%)
	FD3	7.6	α_L=250, α_T=130	0.1	**0.5**	60°	37.7 (0.38%)
	FD4	7.6	α_L=250, α_T=130	0.1	**0.5**	90°	37.7 (0.38%)
Dispersivity coefficient	Alf1	7.6	α_L=180, α_T=90	0.1	**0.5**	0°	50.3 (0.50%)
	Alf2	7.6	α_L=120, α_T=60	0.1	**0.5**	0°	50.3 (0.50%)
Aquifer Heterogeneity	H1	Shown in Figure S17	α_L=250, α_T=130	0.1	**0.5**	0°	37.7 (0.38%)

Notes:

[a] Flow direction is angle of flow direct count–wise to the X-axis shown in Figure S1 and the insert of Figure S18a.

[b] Numbers in parentheses represent percent of total CO_2 mass stored in the deep reservoir (10 MM ton assumed in this study) leaked over 1000 years.

[c] Brine is leaked into the aquifer with chemical compositions listed in Table S2.

[d] Leakage location (P&A well) is located in the model domain shown in Figure S4.

[e] Parameters in LR4 are the same as those in J2 for consistently naming those simulations.

S3. Impacts of dispersion coefficient, groundwater flow direction, and aquifer heterogeneity on monitoring efficiency of a monitoring network at the CO_2-EOR site

Because the dispersion coefficient can affect the lateral and longitudinal extension of a CO_2 plume in an aquifer, three runs were conducted to evaluate impacts of the dispersion coefficient on monitoring efficiency (ME); impacts of the dispersion coefficient appear to be negligible (Figure S13).

Four runs with groundwater flow direction (θ) ranging from 30^o to 90^o (insert of Figure S14a) were conducted. GMN1 has the lowest ME for $\theta = 0^o$ and the greatest ME for $\theta = 60^o$ (Figure S14a), while GMN7 has the greatest ME for $\theta = 45^o$ and the smallest ME for $\theta = 60^o$ (Figure S14b), suggesting that groundwater-flow direction should be considered for a GMN design.

A preliminary simulation was conducted to assess impacts of aquifer heterogeneity on ME. Stochastic realization of log K in the shallow aquifer was simulated with GCOSIM3D,[4] a sequential multi-Gaussian random function simulator. Log K is assumed to be a random Gaussian function having a spherical semivariogram, γ (h), given by [5]:

$$\gamma(h) = \begin{cases} 0.5S\left[\left(\frac{h}{a}\right) - \left(\frac{h}{a}\right)^3\right] & if\ h < a \\ S & if\ h \geq a \end{cases}$$

where a and S are the range and sill, respectively, and h is the distance.

Because there is very limited data about spatial distribution of hydraulic conductivity in the shallow aquifer, a synthetic hydraulic conductivity was simulated with parameters of a=600 m and S=1.5 and shown in Figure S15. Mean of the hydraulic conductivity is 7.62 m/day (Table S5). The detail procedure to simulate the spatial distribution of hydraulic conductivity with GCOSIM3D can also be found in Yang and Samper (2009)[5]. Note that more realistic data about spatial distribution of hydraulic conductivity should be used in a future study. Comparison of ME in the homogeneous and heterogeneous aquifers shows that aquifer heterogeneity has impacts on ME (Figure S16). However, because a single realization of aquifer heterogeneity was simulated, multiple realizations of aquifer heterogeneity may be conducted for further understanding of the impacts of aquifer heterogeneity on ME.

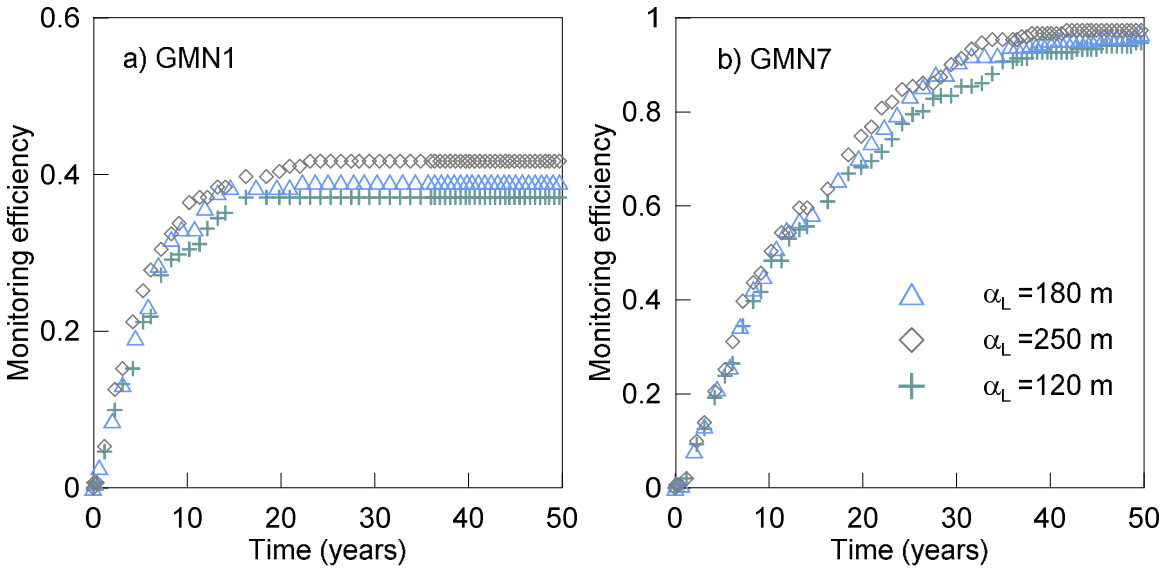

Figure S13. Comparison of monitoring efficiency with (a) GMN1, and (b) GMN7 for dissolved CO_2, with different longitudinal dispersion coefficients, α_L. (Note that the ratio of the longitudinal dispersion coefficient to the transverse dispersion coefficient keeps constant, 2 for the three runs.)

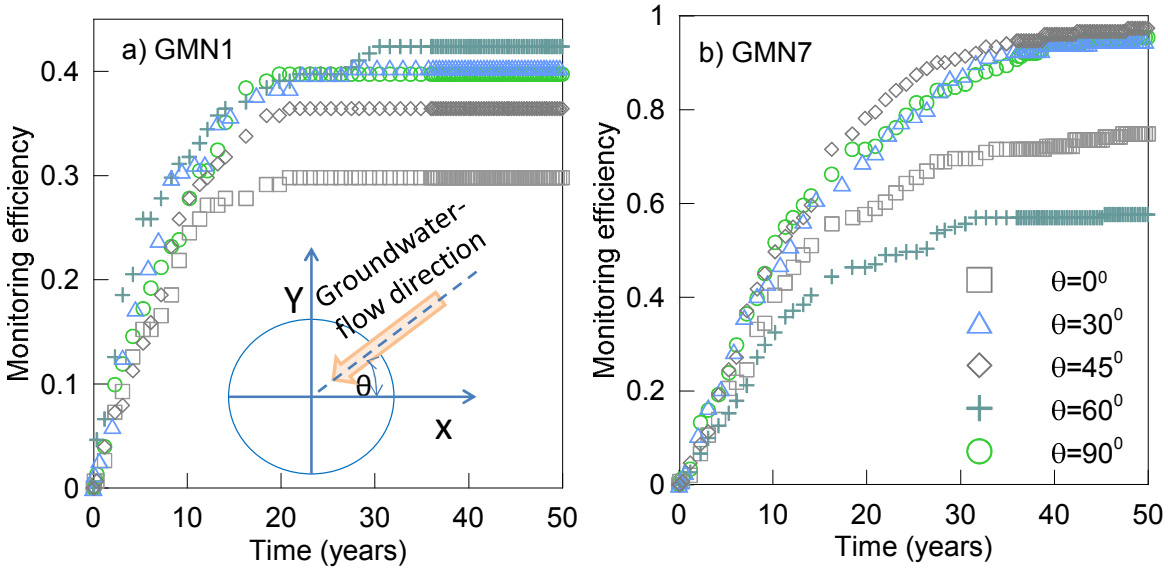

Figure S14. Comparison of monitoring efficiency of (a) GMN1, and (b) GMN7, with dissolved CO_2 for different groundwater-flow directions in the numerical simulations (Table S5).

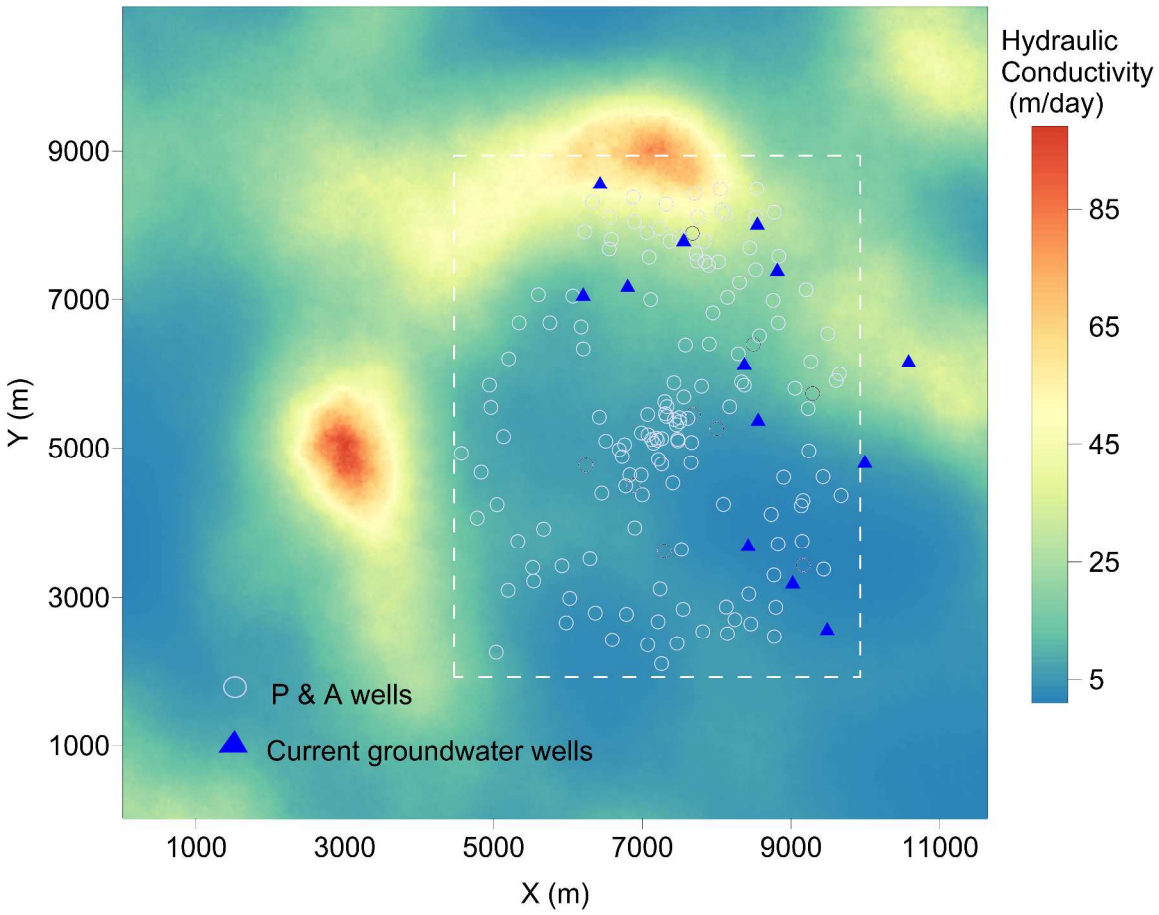

Figure S15. Spatial distribution of hypothetic hydraulic conductivity field (m/day) used in the numerical simulation to consider impacts of aquifer heterogeneity on the monitoring efficiency of the nine monitoring networks shown in Figure 1. Note that the hydraulic field in the simulation run does not necessarily represent the real hydraulic conductivity in the regional aquifer of the study area.

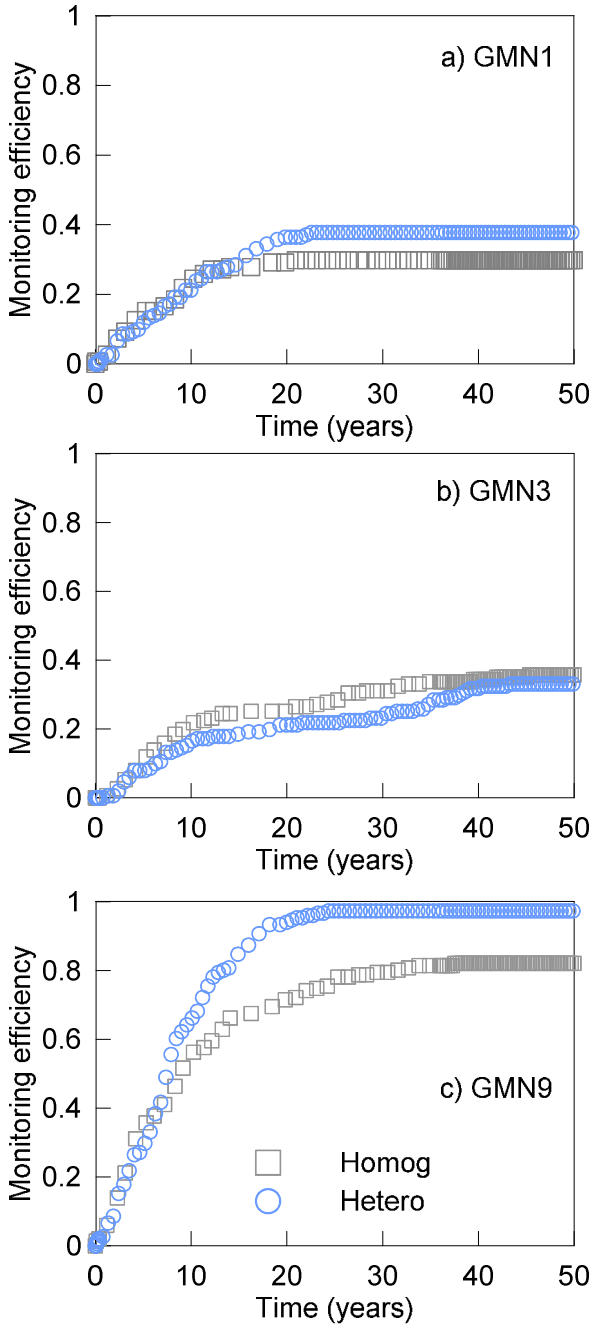

Figure S16. Comparison of monitoring efficiency with (a) GMN1, (b) GMN3, and (c) GMN9 for dissolved CO_2 in homogeneous and heterogeneous aquifers. (Distribution of hydraulic conductivity is shown in Figure S15.)

References Cited in Supplementary Materials

1. Hounslow, A., *Water quality data: analysis and interpretation*. Lewis publishers: New York, 1995; p 397.
2. Parkhurst, D. L.; Appelo, C. A. J. *User's guide to phreeqc (version 2)— a computer program for speciation, batch-reaction, one-dimensional transport, and inverse geochemical calculations*; Water-Resources Investigations Report 99-4259; U.S. Geological Survey 1999; p 310.
3. Lu, J.; Kharaka, Y. K.; Thordsen, J. J.; Horita, J.; Karamalidis, A.; Griffith, C.; Hakala, J. A.; Ambats, G.; Cole, D. R.; Phelps, T. J.; Manning, M. A.; Cook, P. J.; Hovorka, S. D., CO2–rock–brine interactions in Lower Tuscaloosa Formation at Cranfield CO2 sequestration site, Mississippi, U.S.A. *Chemical Geology* **2012,** *291*, (0), 269-277.
4. Gómez-Hernández, J. J.; Journel, A., Joint Sequential Simulation of MultiGaussian Fields. In *Geostatistics Tróia '92*, Soares, A., Ed. Springer Netherlands: 1993; Vol. 5, pp 85-94.
5. Yang, C.; Samper, J., Numerical evaluation of multicomponent cation exchange reactive transport in physically and geochemically heterogeneous porous media. *Computational Geosciences* **2009,** *13*, (3), 391-404.